Analysis and Optimization of the Efficiency of Induction Heating Applications With Litz-Wire Planar and Solenoidal Coils

Ignacio Lope, *Student Member, IEEE*, Jesús Acero, *Member, IEEE*, and Claudio Carretero, *Member, IEEE*

***Abstract*—Optimization of the efficiency of an induction heating application is essential in order to improve both reliability and performance. For this purpose, multistranded cables with litz structure are often used in induction heating applications. This paper presents an analysis and optimization of the efficiency of induction heating systems focusing on the optimal copper volume of the winding with respect to different constraints. The analysis is based on the concept of a one-strand one-turn coil, which captures the dissipative effects of an induction heating system and reduces the number of variables of the analysis. An expression for the efficiency of the induction heating system is derived. It is found that, with the geometry and the other parameters of the system fixed, efficiency depends on the copper volume of the windings. In order to use this result to optimize the efficiency of an application, volume restrictions, the packing factor and the window utilization factor are also considered. The optimum frequency for an induction heating system is also studied in this study. An experimental verification for both planar and solenoidal cases is also presented.**

***Index Terms*—Electromagnetic analysis, induction heating, loss optimization.**

I. Introduction

INDUCTION heating technology is applied in many different fields, ranging from medical [1], [2] to industrial uses [3]. Its advantages include efficient and rapid heating as well as electrical isolation. The basic arrangement of an induction heating system consists of an ac source feeding a coupled coil-target system. Usually, coils are arranged in several turns following an axisymmetric geometry adapted to the shape of the induction target. In industrial systems, solenoid-type induction systems are the most common [4], [5], whereas in medical and residential applications, planar arrangements are preferred [6], [7]. An illustration of these arrangements is depicted in Fig. 1.

Manuscript received April 29, 2015; revised August 21, 2015; accepted August 31, 2015. Date of publication September 10, 2015; date of current version January 28, 2016. This work was supported in part by the Spanish MINECO under Project TEC2013-42937-R, Project CSD2009-00046, and Project RTC-2014-1847-6, in part by the FPU Grant AP2010-4446, in part by the DGA-FSE, in part by the University of Zaragoza under Project JIUZ-2014-TEC-08, and in part by the BSH Home Appliances Group. Recommended for publication by Associate Editor C. Sullivan.

I. Lope is with the Departmento de Ingeniería Electrónica y Comunicaciones, Universidad de Zaragoza, María de Luna 1, 50018 Zaragoza, Spain and also with BSH Home Appliances Spain, Avenida de la Industria 49, 50016 Zaragoza, Spain (e-mail: nlope@unizar.es).

J. Acero is with the Departmento de Ingeniería Electrónica y Comunicaciones, María de Luna 1, 50018 Zaragoza, Spain (e-mail: jacero@unizar.es).

C. Carretero is with the Departamento de Física Aplicada. Universidad de Zaragoza, Pedro Cerbuna 12, 50009 Zaragoza, Spain (e-mail: ccar@unizar.es).

Color versions of one or more of the figures in this paper are available online at http://ieeexplore.ieee.org.

Digital Object Identifier 10.1109/TPEL.2015.2478075

Fig. 1. Typical induction heating arrangements. (a) Planar. (b) Solenoidal.

The designs of induction heating coils depend on several factors, for example, rated power, minimum loss, size, temperature, weight, or a combination of these. Historically, copper tubes have been used in the industrial induction heating sphere, because they meet the specific requirements of frequency (up to several megahertz), power (up to hundreds of kilowatt) or temperature (800 °C or higher) with a moderate cost. On the other hand, the litz wire is the cable of choice in residential applications, such as induction cookers, mainly due to the optimal balance between efficiency and cost. Nowadays, the growing concern about efficient power conversion makes the litz wire an interesting option not only for residential applications but also for industrial applications at the medium range of frequency, power, or temperature.

Considering these potential applications, it is important to bear in mind temperature limitations of the litz wire, which depends on the working temperature of the insulation materials. Therefore, litz wire coils could not be appropriate for some induction heating applications as melting, forging, or brazing because radiant or convection heating of the coil may exceed its limit temperature. However, there are other industrial applications, as the sealing of cans by means of aluminum caps, where a litz wire could be an interesting option. Moreover, a litz wire could be also used in combination with appropriate low-emissive bobbins (such as ceramic materials) with moderate temperature increase due the radiation of the workpiece.

The litz wire has been object of study in many papers, mainly with the aim of loss modeling [8]–[13] and optimal design [14]–[18] of inductors and transformers for switch-mode power supplies (SMPS). Comparatively, the number of studies devoted to litz-wire windings for induction heating applications is small, which in part is due to the fact that the sphere of use and market for SMPS are quite different from those of induction heating. The existing works in the field of induction heating are mainly

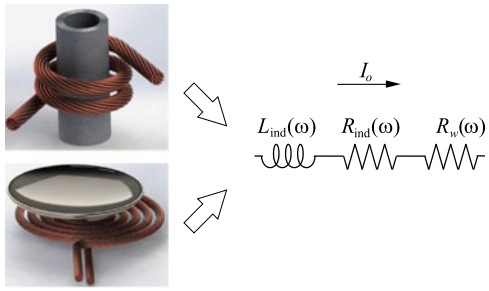

Fig. 2. Equivalent circuit of induction heating systems.

focused on loss modeling [19], [20] and efficiency analysis [21]. The studies mentioned previously for SMPS could to a greater or a lesser extent be applied to induction heating and they are undoubtedly a valuable starting point. However, coils for induction heating systems have several differences compared to the magnetic components of SMPS, and therefore, there is room for further contributions, especially in the field of the efficiency-oriented design.

The design of inductors and transformers is often focused on the minimization of winding losses, which can be accomplished by an appropriate selection of the number and radius of the strands, while considering other restrictions such as the total volume or cost. However, the design of induction heating coils should rather be focused on the efficiency of energy transference, which depends on both the dissipation in the workpiece and the losses of the windings. In an induction system, these dissipations are not decoupled: rather, both depend on the global magnetic field of the specific application and the frequency, being of special importance the frequency dependence, which should be accounted for in order to optimize the induction heating system.

The winding volume of inductors and transformers for SMPS is usually closely related to the size of the bobbin and the core. The design tools developed by manufacturers or researchers [16] often includes a list of the standard bobbins in order to check if the volume occupied by the windings of the designs fits in a specific bobbin. In the induction heating field, the winding volume mainly depends on the available space in each specific application, and sometimes this is a major restriction, which makes the design more difficult. For example, in domestic induction heating appliances (both conventional [22] or total active surfaces [23]), the assembly of coils and power electronics in the housing imposes severe volume restrictions that are reflected in the design of the inductors. Volume restrictions become more evident in printed circuit board implementations of planar windings with the litz-wire structure [24], [25] and microfabricated inductors [26], [27]. In other applications, the dissipated heat must be concentrated in a small area, and therefore, the coil should be adapted to the heating zone.

Considering the aforementioned differences, in this paper, we present a study on induction heating systems with the litz wire focusing on the optimization of the efficiency with respect to the copper volume. Different restrictions such as the operating frequency, the window area utilization or the radius of the strands are also considered. For this purpose, a semianalytical method combining finite-element (FEA) field simulations and formulas for calculating the loss is followed. This paper is organized as follows. In Section II, an electromagnetic analysis of the efficiency of an induction heating system is presented. Section III describes the design issues. Section IV presents an experimental verification of the proposed model, and Section V summarizes the findings of this study.

II. Electromagnetic Analysis of the Induction Heating Efficiency

The most common electrical model of an induction heating system consists of an inductance, L_{ind}, and resistance, R, connected in series, as is shown in Fig. 2. The resistance is often divided in the induced resistance term, R_{ind}, and the resistance of the winding, R_w [28].

The inductive efficiency of an inductor system is defined as the ratio between the power transferred to the target, P_{ind}, with respect to the total electrical power supplied to the coil, P_{supplied}. In terms of resistances, the induction efficiency can be expressed as follows [21]:

$$\eta_{\text{ind}} = \frac{P_{\text{ind}}}{P_{\text{supplied}}} = \frac{\frac{1}{2} I_o^2 R_{\text{ind}}}{\frac{1}{2} I_o^2 R} = \frac{R_{\text{ind}}}{R_{\text{ind}} + R_w} \tag{1}$$

where I_o is the current of the coil, R_{ind} represents the inductive power transferred to the target, and R_w the power dissipated in the windings. These resistances are modeled in the following sections by means of FEA field simulations of the induction heating system. From these simulations, the induced impedance of an ideal-winding induction heating system, Z_{ind}, is extracted. The winding resistance, R_w, is calculated by combining these simulations with the ac loss model of the real cable.

A. Electromagnetic Modeling of the Induction Heating

Rectangular cross-sectional coils of rotational symmetry are considered in this analysis. This geometry corresponds to the planar and solenoidal arrangements schematically represented in Fig. 3(a) and (b), where r_{int} and r_{ext} are the internal and external radii of the coil, respectively; and t the thickness. It is assumed that the coils consist of n equally distributed turns that are compactly wound with a litz wire of n_s isolated strands of radius r_w. It is important to note that the number of turns, n, and number of strands, n_s, are constrained by several factors, as the packing factor of the isolated strands. This effect is later separately accounted for with design purposes

Thus, considering the properties of an ideal litz wire (i.e., a multistranded wire whose strands are equivalent), the electrical current can be assumed to be uniformly distributed over the entire cross-sectional area of the winding, S_{winding}, in the required frequency range. Consequently, the coils can be assumed to an ideal conducting media, i.e., null conductivity $\sigma = 0$, which are modeled in the FEA simulations by the following constant current density $\mathbf{J}_{\text{coil}}$:

$$\mathbf{J}_{\text{coil}} = \frac{I_o}{S_{\text{turn}}} \hat{\boldsymbol{\varphi}} = n \frac{I_o}{S_{\text{coil}}} \hat{\boldsymbol{\varphi}} = n \frac{I_o}{t\,(r_{\text{ext}} - r_{\text{int}})} \hat{\boldsymbol{\varphi}} \tag{2}$$

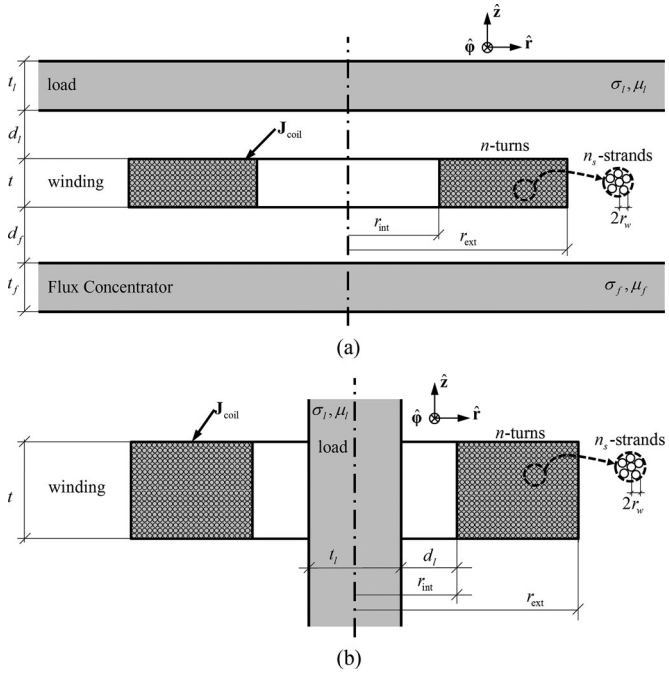

Fig. 3. Typical induction heating arrangements. (a) Planar coil in transverse flux configuration. (b) Solenoidal coil in longitudinal flux configuration.

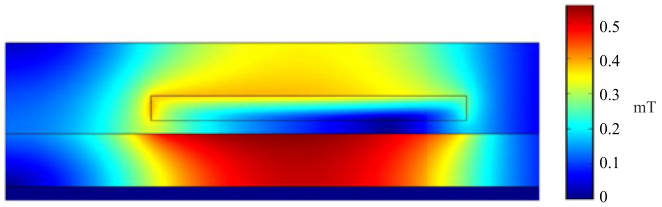

Fig. 4. Magnetic flux density extracted from FEA field simulations of a winding placed between a ferromagnetic medium acting as a load and a flux concentrator.

where $\hat{\varphi}$ is the unit vector representing the Azimuthal direction of the system, $S_{\rm turn}$, $S_{\rm coil}$ are the turn and the coil cross-sectional areas, respectively.

The workpiece and the flux concentrator (a ferrite for the planar configuration) are also included in the system. These media are characterized by means of the electrical conductivity σ_k and magnetic permeability μ_k, where *k* could be the load or the ferrite. In this analysis, the ferrite is considered a loss-free medium. Geometrical parameters and distances from the media to the coils are also represented in Fig. 3 (a) and (b). In order to be illustrative, an FEA field simulation of a planar arrangement is represented in Fig. 4, where the workpiece has been replaced by the impedance boundary condition [29].

B. Analysis of Inductive Power Transferred to the Target

The induced equivalent impedance $Z_{\rm ind}$ of these systems is defined as $Z_{\rm ind} = V_{\rm ind}/I_o$, where $V_{\rm ind}$ is the induced voltage of the ideal loss-free coils. Neglecting capacitive effects, $Z_{\rm ind}$ is modeled as a resistance in series with an inductance, i.e., $Z_{\rm ind} = R_{\rm ind} + j\omega L_{\rm ind}$, where $R_{\rm ind}$ represents the inductive power transferred to the target and $L_{\rm ind}$ represents the magnetic field of the system.

Voltage $V_{\rm ind}$ is the integral of the Azimuthal electric field, E_φ, along the projection of the coil. Taking into account the axial symmetry and also considering that the coil consists of *n* equally distributed turns, the induced voltage is obtained by integrating E_φ over the entire coil volume divided by the cross-sectional area $S_{\rm coil}$ and multiplied by the number of turns *n*. Therefore, $V_{\rm ind}$ becomes

$$V_{\rm ind} = -\oint_{\rm winding} \mathbf{E}\cdot\mathbf{dl} = -\frac{n}{S_{\rm coil}}\int_{r_{\rm int}}^{r_{\rm ext}}\int_0^t 2\pi r E_\varphi dz dr \tag{3}$$

where E_φ is obtained from the FEA simulations and *r* is the radial coordinate.

Regarding the equivalent impedance, the number of turns of the coil is of especial relevance. In order to parameterize the number of turns, it is convenient to consider coils with only one turn, i.e., $n = 1$, and the same geometries of those presented in Fig. 3. These coils are here called as one-turn coils. Let $E_{\varphi,1}$ be the electric field generated by a one-turn coil. Therefore, the corresponding one-turn voltage $V_{\rm ind,1}$ is

$$V_{\rm ind,1} = -\frac{1}{S_{\rm coil}}\int_{r_{\rm int}}^{r_{\rm ext}}\int_0^t 2\pi r E_{\varphi,1} dr dz. \tag{4}$$

It is worth to note that the length of the one-turn coil corresponds to the average length of the turns of the coil, also called MLT which is defined as

$$\text{MLT} = \frac{1}{S_{\rm coil}}\int_{r_{\rm int}}^{r_{\rm ext}}\int_0^t 2\pi r dr dz = \pi\left(r_{\rm ext} + r_{\rm int}\right). \tag{5}$$

Assuming linearity of the media, the field E_φ of (3) can be calculated as $E_\phi = nE_{\phi,1}$ Therefore, (3) can be rewritten as follows:

$$V_{\rm ind} = n\cdot n\underbrace{\left[-\frac{1}{S_{\rm coil}}\int_{r_{\rm int}}^{r_{\rm ext}}\int_0^t 2\pi r E_{\varphi,1} dr dz\right]}_{V_{\rm ind,1}} = n^2 V_{\rm ind,1}. \tag{6}$$

Therefore, the impedance of the loss-free coil is

$$Z_{\rm ind} = n^2\frac{V_{\rm ind,1}}{I_0} = n^2 Z_{\rm ind,1} = n^2 R_{\rm ind,1} + j\omega n^2 L_{\rm ind,1} \tag{7}$$

where $Z_{\rm ind,1}$, $R_{\rm ind,1}$, and $L_{\rm ind,1}$ are the impedance, resistance, and inductance of the one-turn coil, respectively.

C. Analysis of Dissipation in the Windings

The winding loss model is based on the decomposition in dc, skin, and proximity losses [30]. Therefore, associating losses to resistances, the winding resistance, R_w, is

$$R_w = R_{\rm cond} + R_{\rm prox} \tag{8}$$

where $R_{\rm cond}$ includes the dc and *skin* resistances (here called *conduction resistance*), and $R_{\rm prox}$ corresponds to the proximity losses induced by the coil itself.

In this case, regarding R_w, the number of strands of the wire is also of especial relevance. Considering ideal litz-wire structure (i.e., equivalence of strands), it is also convenient to consider

TABLE I
IMPEDANCE COMPONENTS

Component	Symbol	Expression	One-Turn Equivalent Coil of One-Strand
Induction impedance	$Z_{\rm ind}$	$Z_{\rm ind} = n^2 Z_{ind,1}$	$Z_{\rm ind,1} = -\frac{1}{S_{\rm coil}} \int_{r_{\rm int}}^{r_{\rm ext}} \int_0^t 2\pi r E_{\varphi,1} dS$
Conduction resistance	$R_{\rm cond}$	$R_{\rm cond} = \frac{n}{n_s} R_{\rm cond,11}$	$R_{\rm cond,11} = \frac{l_{\rm turn}}{\pi r_w^2 \sigma_w} \Phi_{\rm cond}\left(\frac{r_w}{\delta_w}\right)$
Proximity resistance	$R_{\rm prox}$	$R_{\rm prox} = n^3 n_s R_{\rm prox,11}$	$R_{\rm prox,11} = \frac{4\pi}{\sigma_w} \Phi_{\rm prox}\left(\frac{r_w}{\delta_w}\right) \left\langle 2\pi r \left\lvert \bar{\mathbf{H}}_{o,1} \right\rvert^2 \right\rangle_{S_{\rm coil}}$

the number of strands as a parameter. Therefore, the analysis of R_w is carried out for wires with one strand, $n_s = 1$. Taking into account the parameterization with respect to the number of turns of the previous section, in this section, the loss analysis of the coil is carried out on the basis of the one-strand one-turn coil.

The conduction resistance per unit length of a round strand of radius r_w is

$$R_{\rm cond\ u.l.} = \frac{1}{\pi r_w^2 \sigma_w} \Phi_{\rm cond}\left(r_w/\delta_w\right) \tag{9}$$

where $\sigma_{\rm w}$ is the conductor conductivity. The skin depth of the conductor is $\delta_w = (\pi \mu_0 \sigma_w f)^{-1/2}$, μ_0 being the free-space permeability, and f the frequency. The function $\Phi_{\rm cond}(r_w/\delta_w)$ includes the geometry and frequency dependences of the skin losses. For the case of an isolated and widely spaced round strand, an exact expression of $\Phi_{\rm cond}(r_w/\delta_w)$ expressed in terms of Bessel functions has been known for years [31], [32]. For closely packed multistranded wires, this function is not exact, but a small discrepancy is observed for strand diameters equal to or lesser than skin depth [14].

Let $R_{\rm cond,11}$ be the dc and skin resistance of the one-strand one-turn coil of strand radius r_w. Considering that the length of this turn is the coil volume divided by the cross-sectional area (i.e., the MLT) and applying (9), $R_{\rm cond,11}$ is

$$R_{\rm cond,11} = \frac{1}{\pi r_w^2 \sigma_w} \Phi_{\rm cond}\left(r_w/\delta_w\right) \cdot \underbrace{\frac{1}{S_{\rm coil}} \int_{r_{\rm int}}^{r_{\rm ext}} \int_0^t 2\pi r dr dz}_{\rm MLT}. \tag{10}$$

Assuming equivalence of the strands and also assuming a strand radius equal to or lesser than skin depth, the cable can be considered as the parallel of n_s equivalent strands. Moreover, the coil can be considered as the series connection of n turns of the MLT length. Therefore, $R_{\rm cond}$ is

$$R_{\rm cond} = \frac{n}{n_s} R_{\rm cond,11} = \frac{n}{n_s} \frac{\rm MLT}{\pi r_w^2 \sigma_w} \Phi_{\rm cond}\left(r_w/\delta_w\right). \tag{11}$$

A similar analysis for the proximity resistance, $R_{\rm prox}$, can be carried out. The proximity resistance per unit length of a round strand of radius r_w can be written as

$$R_{\rm prox\ u.l.} = \frac{4\pi}{\sigma_w} \Phi_{\rm prox}\left(r_w/\delta_w\right) \left\lvert \bar{\mathbf{H}}_o \right\rvert^2 \tag{12}$$

where $\left\lvert \bar{\mathbf{H}}_o \right\rvert$ is the spatial average of the transverse magnetic field applied to the strand for a coil current $I_o = 1$ A. For the systems of Fig. 3(a) and (b), the value of $\left\lvert \bar{\mathbf{H}}_o \right\rvert^2$ at any point can be calculated by FEA and depends on the surrounding media. The geometry and frequency dependences of the proximity resistance are included in the function $\Phi_{\rm prox}(r_w/\delta_w)$, which includes Bessel functions. For isolated and widely spaced round strands an exact expression of $\Phi_{\rm prox}(r_w/\delta_w)$ with Bessel functions is also known [31], [32].

Let $R_{\rm prox,11}$ be the proximity resistance of the one-strand one-turn coil of strand radius r_w. This resistance can be calculated by applying (12), which requires $\left\lvert \bar{\mathbf{H}}_{o,1} \right\rvert^2$, i.e., the spatial average of the field generated by the one-turn coil at the positions of the coil. This value is obtained by integrating $2\pi r \left\lvert \bar{\mathbf{H}}_{o,1} \right\rvert^2$ on the coil volume and dividing by the cross-sectional area

$$R_{\rm prox,11} = \frac{4\pi}{\sigma_w} \Phi_{\rm prox}(r_w/\delta_w) \frac{1}{S_{\rm coil}} \int_{S_{\rm coil}} 2\pi r \left\lvert \bar{\mathbf{H}}_{0,1} \right\rvert^2 dr dz. \tag{13}$$

Assuming linearity of the media, $\bar{\mathbf{H}}_o$ can be expressed as the field generated by the one-strand one-turn coil, $\bar{\mathbf{H}}_{o,1}$, multiplied by the number of turns, i.e., $\bar{\mathbf{H}}_o = n\bar{\mathbf{H}}_{o,1}$. Moreover, as in the previous section, the cable is considered as the parallel of $n_{\rm s}$ strands and the coil is the series connection of n equally distributed turns. Therefore

$$\begin{aligned} R_{\rm prox} &= n^3 n_s \frac{4\pi}{\sigma_w} \Phi_{\rm prox}\left(r_w/\delta_w\right) \left\langle 2\pi r \left\lvert \bar{\mathbf{H}}_{o,1} \right\rvert^2 \right\rangle_{S_{\rm coil}} \\ &= n^3 n_s R_{\rm prox,11} \end{aligned} \tag{14}$$

where $\left\langle 2\pi r \left\lvert \bar{\mathbf{H}}_{o,1} \right\rvert^2 \right\rangle_{S_{\rm coil}}$ is the mean value of $2\pi r \left\lvert \bar{\mathbf{H}}_{o,1} \right\rvert^2$ in the cross-sectional area of the coil being this value extracted from FEA simulations.

It is worth noting several aspects of the last equation. First, the magnetic field $\bar{\mathbf{H}}_{o,1}$ is frequency dependent because conductive media are present in the system. Second, according to the ideal model coil adopted, $\bar{\mathbf{H}}_{o,1}$ is not affected by the self-induced currents in the coil conductors. This assumption is potentially valid if cables with enough stranding level are used. Third, considering that $\Phi_{\rm prox}(r_w/\delta_w)$ of (14) is only valid for isolated and widely spaced round strands, this equation cannot be considered as exact. However, the approximation (14) is valid if the strand radius is equal to or lesser than skin depth. Some authors have further evaluated this approximation [12].

The impedance contributions in induction heating systems and their dependences with respect to n and $n_{\rm s}$ are summarized in Table I.

D. Low-Frequency Resistance Approximation

In a specific design, the optimization of the strand diameter, the number of strands, or the operating frequency is usually required. However, it is cumbersome to extract practical values from (11) and (14) due to the fact that $\Phi_{\rm cond}(r_w/\delta_w)$ and $\Phi_{\rm prox}(r_w/\delta_w)$ include Bessel functions. Several authors have proposed alternative simplified expressions to calculate the ac loss in multistranded cables [13], [33], [34]. Another possibility is to take approximations based on the asymptotic tendencies of $\Phi_{\rm cond}(r_w/\delta_w)$ and $\Phi_{\rm prox}(r_w/\delta_w)$ at the low-frequency (LF) and high-frequency (HF) values [35]. At the LF range, it can be proved that

$$\begin{aligned}\Phi^{\rm LF}_{\rm cond}(r_w/\delta_w) &= 1 \qquad\qquad r_w/\delta_w < 1\\ \Phi^{\rm LF}_{\rm prox}(r_w/\delta_w) &= 1/4(r_w/\delta_w)^4 \;\; r_w/\delta_w < 1.\end{aligned} \tag{15}$$

The resistances for the one-strand one-turn equivalent coil become

$$\begin{aligned}R^{\rm LF}_{\rm cond,11} &= R_{\rm DC,11} = \frac{1}{\sigma_w}\frac{\rm MLT}{\pi r_w^2} \qquad\qquad r_w/\delta_w < 1\\ R^{\rm LF}_{\rm prox,11} &= \pi/\sigma_w \cdot \left\langle 2\pi r \left|\bar{\mathbf{H}}_{o,1}\right|^2 \right\rangle_{S_{\rm coil}} \cdot (r_w/\delta_w)^4 \;\; r_w/\delta_w < 1.\end{aligned} \tag{16}$$

Taking into account the assumptions of uniform current coil distribution and strand radius equal to or lesser than skin depth, the LF approximation is used in order to obtain practical and simple equations for the design of induction heating systems.

Concluding this section, the main approximations adopted in the presented modeling are summarized. An ideal winding modeled as a constant current density is considered to solve the fields in the induction heating system as well as linear materials and loss-free flux concentrators are assumed, which allows using the Fourier series to obtain the current for any periodic voltage waveform. The ac loss model of the winding assumes ideal litz-wire structure, neglecting losses associated with the bundle-level effects. Isolated and widely spaced round strands are assumed in the modeling of the frequency-dependent winding losses. This assumption is especially suited for reduced-size strands compared to the skin depth being the LF approximation adequate.

III. Efficiency-Oriented Design

A study of the induction efficiency has been carried out, focusing on the optimization of the induction efficiency with respect to some practical parameters such as the operation frequency, the winding parameters, the copper volume, and the packing factor of the wires.

A. Induction Efficiency and Coil Volume Dependence

Considering the previous modeling and applying (1), (7), (8), (11), and (14), the induction efficiency can be expressed as

$$\eta_{\rm ind} = \frac{R_{\rm ind,1}}{R_{\rm ind,1} + 1/nn_s R_{\rm cond,11} + nn_s R_{\rm prox,11}}. \tag{17}$$

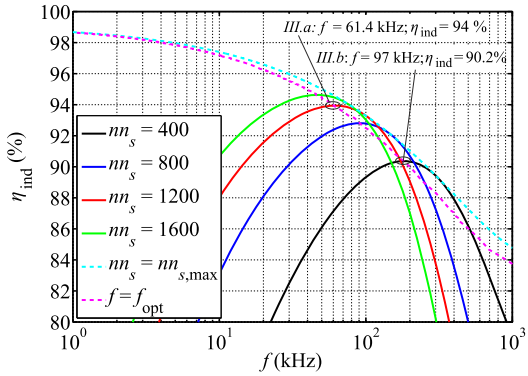

Fig. 5. Induction efficiency with respect to the frequency for different factors nn_s (continuous line), for the optimum value of $nn_s = nn_{s,\max}$ (dashed cyan line) and with respect to the optimum frequency $f = f_{\rm opt}$ for given nn_s and wire radius r_w (dashed magenta line). The system corresponds to a solenoidal coil with $r_w = 0.1$ mm with a ferromagnetic load in longitudinal flux configuration.

According to this expression, induction efficiency depends on the resistances corresponding to the one-strand one-turn coil, $R_{\rm ind,1}$, $R_{\rm cond,11}$, $R_{\rm prox,11}$ (which includes the frequency-dependency) and the factor nn_s, i.e., the number of turns multiplied by the number of strands. It can also be deduced that the induction efficiency depends on the copper volume defined as $V_{\rm Cu} = nn_s \pi r_w^2 \,{\rm MLT}$.

Therefore, if the system geometry, the wire radius r_w and the operating frequency are fixed, different coils with the same result of the number of turns multiplied by the number of strands, nn_s, (i.e., coils with the same copper volume) have the same efficiency. Fig. 5 shows the induction efficiency for different $nn_{\rm s}$ factors (continuous line) with respect to the frequency for a given wire radius ($r_w = 0.1$ mm).

In the following sections, (17) is used to optimize the induction efficiency for design purposes.

B. Condition of Maximum Efficiency

When the winding area without geometrical restrictions, the frequency and the wire radius r_w are fixed, the solution of $\partial\eta_{\rm ind}/\partial(nn_s) = 0$ gives the nn_s, which maximizes the induction efficiency. It is worth noting that, in this case, the maximum winding area is not restricted by the winding area of a bobbin (which is associated to a magnetic core) as occurs in SMPS. Rather, it depends on the specific induction heating application. According to (17), the following condition is obtained:

$$nn_{s,\max} = \sqrt{R_{\rm cond,11}/R_{\rm prox,11}}. \tag{18}$$

The same condition can be obtained if $R_{\rm cond} = R_{\rm prox}$ or, in other words, if the optimum efficiency occurs when the conduction (dc+skin) equals the proximity resistances. This result has also been found by other authors, as can be seen in several works concerning the litz-wire transformer winding [14]. The maximum induction efficiency $\eta_{\rm ind,max}$ for a given system is represented by the dashed cyan line in Fig. 5, which corresponds to the envelope of the set of curves obtained for different values of $nn_{\rm s}$. This envelope was numerically obtained, and subsequently,

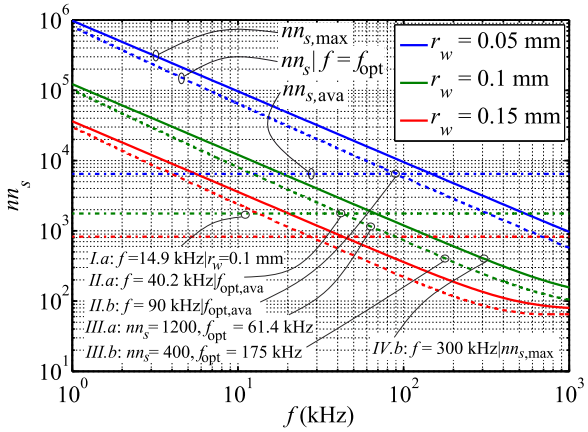

Fig. 6. Factor $nn_{s,\max}$ that maximizes the efficiency as a function of the frequency for different strand radii (continuous line). Factor nn_s that maximizes the efficiency at $f_{\rm opt}$ for different strand radii (dashed line). Available $nn_{s,\rm ava}$ for the solenoidal configuration of Table III (dashed line of constant value)

represented. Nevertheless, $\eta_{\rm ind,max}$ can be analytically obtained by applying the result (18) in (17) giving

$$\eta_{\rm ind,max} = \frac{R_{\rm ind,1}}{R_{\rm ind,1} + 2\sqrt{R_{\rm cond,11} R_{\rm prox,11}}}. \tag{19}$$

Fig. 6 shows the factor $nn_{s,\max}$ by continuous line as a function of frequency for different strand radii. As is shown, at an LF regime, the higher the frequency, the lower the $nn_{s,\max}$. In other words, for the same strand radius, an increase in the frequency allows either the number of turns or the number of strands to be reduced achieving the maximum efficiency. At an HF regime, $nn_{s,\max}$ is much more constant with respect to the frequency.

Equation (18) gives the theoretical $nn_{s,\max}$ value that maximizes the induction efficiency. However, for design purposes, in order to make the selection of r_w easier, it is more useful to have an expression of $nn_{s,\max}$ in terms of r_w than in terms of $R_{\rm cond,11}$, $R_{\rm prox,11}$ because the latter include Bessel functions among other dependences. Therefore, applying the LF approximation of $R_{\rm cond,11}$, $R_{\rm prox,11}$ (16), $nn_{s,\max}$ is rewritten as follows:

$$nn_{s,\max}^{\rm LF} = \sqrt{\frac{\rm MLT}{\left\langle 2\pi r \left|\bar{\mathbf{H}}_{o,1}\right|^2 \right\rangle_{S_{\rm coil}}}} \frac{1}{\sigma_w \mu_o} \frac{1}{f} \frac{1}{r_w^3}, \quad r_w/\delta_w < 1. \tag{20}$$

Moreover, applying the LF approximation, the maximum inductive efficiency, $\eta_{\rm ind,max}$ is given by

$$\eta_{\rm ind,max}^{\rm LF} = \frac{R_{\rm ind,1}}{R_{\rm ind,1} + \sqrt{\rm MLT \cdot \left\langle 2\pi r \left|\bar{\mathbf{H}}_{o,1}\right|^2 \right\rangle_{S_{\rm coil}}}} \times \frac{1}{\mu_0 \omega r_w}, \quad r_w/\delta_w < 1. \tag{21}$$

C. Frequency Design for Maximum Efficiency

Equation (18) provides the factor $nn_{s,\max}$, which maximizes $\eta_{\rm ind}$. According to the results presented in Fig. 5, it may seem that the maximum efficiency of a design can be achieved by simply selecting the appropriate $nn_{s,\max}$ at a given frequency using the envelope of the $\eta_{\rm ind,max}$, which is represented by the cyan curve. However, in some cases, the factor nn_s could be fixed for different reasons, for example, for a fixed number of turns or a fixed number of strands, and the optimization should be performed for a specific nn_s. In these cases, it may also be interesting to obtain the frequency $f_{\rm opt}$ maximizing the inductive efficiency.

Therefore, for a specific nn_s factor, the theoretical frequency $f_{\rm opt}$ at which the maximum efficiency is achieved can be obtained by $\partial\eta_{\rm ind}/\partial f = 0$, where $\eta_{\rm ind}$ is given by (17). Taking into account that several terms of this equation, such as $R_{\rm ind,1}$, $\Phi_{\rm cond}(r_w/\delta_w)$, $\Phi_{\rm prox}(r_w/\delta_w)$, and the magnetic field, are frequency dependent, and therefore, are not straightforwardly derivable with respect to the frequency, the solution of the aforementioned condition has been obtained using post-processing numerical calculations. Fig. 5 shows the $\eta_{\rm ind}$ considering the frequency axis as the $f_{\rm opt}$ for a set of different nn_s values by dashed magenta line. This line corresponds to the peak values of the efficiency curves for different nn_s values and it is represented by a dashed magenta line. It is worth noting that this line is very close but not coincident with the $\eta_{\rm ind,max}$ obtained in the previous section. The difference lies in the fact that $\eta_{\rm ind,max}$ corresponds to the envelope, whereas the $\eta_{\rm ind}$ at the optimal frequency $f_{\rm opt}$ corresponds instead to the peak of the efficiency curves.

Curves of $nn_{\rm s}$ that maximize $\eta_{\rm ind}$ at $f_{\rm opt}$ for different strand radii are also shown in Fig. 6 with slopping dashed lines. As in the previous case, this line is close but not coincident with $nn_{s,\max}$ for the reasons previously commented.

D. Geometry Winding Restrictions

In the previous section, a winding area without any spatial or volume restrictions has been considered. However, the maximum copper volume is usually restricted by several factors that usually are modeled by means of the utilization factor K_u. This factor is defined as the ratio between the copper cross section, $S_{\rm Cu}$, and the coil cross section, $S_{\rm coil}$. Therefore, the actual copper cross section available, $S_{\rm Cu}$, is given by

$$S_{\rm Cu} = K_u \cdot S_{\rm coil}. \tag{22}$$

The window utilization factor depends on the strand radius, the wire insulation, and the packing factor of the winding. In this case, the window utilization factor is defined as the product of the strand insulation factor, K_i, and by the air factor, K_a, i.e., $K_u = K_i \cdot K_a$ [36].

An estimation of K_a is here proposed considering that the turns are arranged according to a square pattern and the strands according to a triangular pattern [36] $K_a \approx (\pi/4)\cdot(\pi/2\sqrt{2})$. Therefore

$$K_u \approx \frac{\pi}{4}\frac{\pi}{2\sqrt{3}}\left(\frac{r_w}{r_w + t_{\rm ins}}\right)^2, \tag{23}$$

where $t_{\rm ins}$ is the insulation thickness. The window utilization factor can be approximated by a power law as follows [14]:

$$K_u = (r_w/r_a)^b. \tag{24}$$

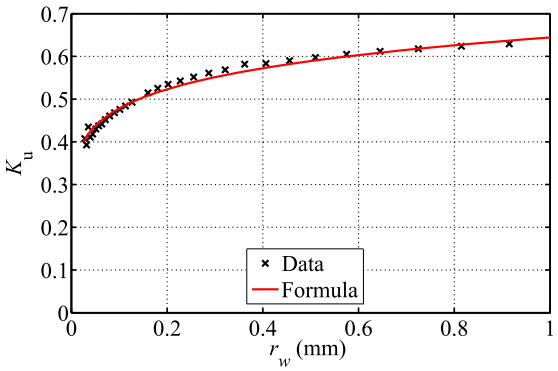

Fig. 7. Copper factor utilization, K_u. Table of [37] (crosses) and (24) approximation (continuous line).

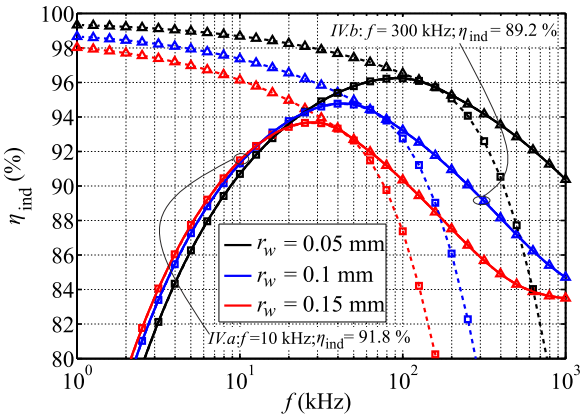

Fig. 8. Frequency-dependent inductive efficiency without winding restrictions, $\eta_{\mathrm{ind,max}}$ (dash line and triangles) and with geometry restrictions $\eta_{\mathrm{ind,ava}}$ (dashed line and squares). The feasible designs correspond to the continuous line.

Parameters $r_a = 0.02979$ m and $b = 0.1295$ have been obtained by means of a curve-fit tool from data provided by the manufacturers for double insulation strands [37]. The manufacturer's curve and the fitted data are compared in Fig. 7. The approximation adopted here only considers simple arrangements that consist of a group of strands bunched and twisted into a bundle. Therefore, it does not take into account more complex constructions consisting of several groups, like those described earlier, which are twisted into higher level bundles. Apart from this consideration, other packing factors can be considered and included by adapting the parameters r_a and b.

Considering the window utilization factor and also considering (22), the available nn_s is

$$nn_{s,\mathrm{ava}} = K_u S_{\mathrm{coil}} / \pi r_w^2. \tag{25}$$

According to Fig. 7, design with small strands have smaller utilization factor. Fig. 6 shows (dashed line of constant value) the $nn_{s,\mathrm{ava}}$ for the solenoidal configuration of the Table III and different strand radii. This value is proportional to the available copper cross section for this specific geometry.

The induction efficiency corresponding to the available copper volume, $\eta_{\mathrm{ind,ava}}$ is obtained by inserting $nn_{s,\mathrm{ava}}$ in (17). Fig. 8 shows both the maximum efficiency without restrictions

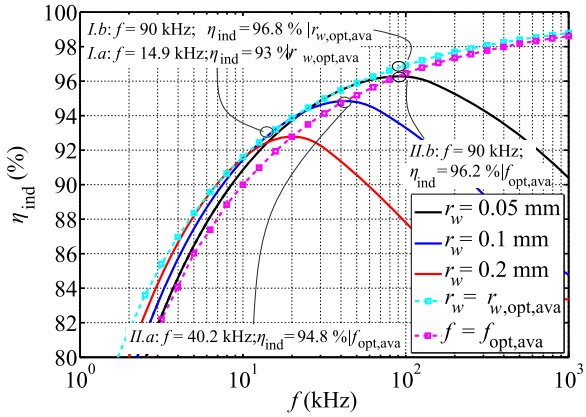

Fig. 9. Induction efficiency for different strand radii considering the winding restrictions, $\eta_{\mathrm{ind,ava}}$ (continuous line). The optimum available efficiency $\eta_{\mathrm{ind,opt,ava}}$ achieved for the best strand radius at each frequency, $r_{w,\mathrm{opt,ava}}$, corresponds to the dashed line and cyan square mark. The available efficiency under geometry restrictions with respect to the optimum frequency $f = f_{\mathrm{opt}}$ is also represented by a magenta dashed line and square mark.

$\eta_{\mathrm{ind,max}}$ and with restrictions $\eta_{\mathrm{ind,ava}}$ for different strand radii. The point where both efficiencies meet corresponds to an optimum design, which takes exactly the available volume. At lower frequencies, the theoretical nn_s would require more space than is available, and therefore, designs with maximum efficiency are not feasible and efficiency decreases. However, at higher frequencies, the theoretical nn_s would require less space than is available, and therefore, the efficiency is coincident with $\eta_{\mathrm{ind,max}}$. In Fig. 8, the curve of feasible designs, composed of sections of the $\eta_{\mathrm{ind,max}}$ and $\eta_{\mathrm{ind,ava}}$ curves, is represented by continuous line.

As has been mentioned, $\eta_{\mathrm{ind,ava}}$ is obtained by considering $nn_{s,\mathrm{ava}}$ in (17). Applying the LF asymptotic approximation, the following available efficiency is obtained:

$$\eta_{\mathrm{ind,ava}}^{\mathrm{LF}} = \frac{R_{\mathrm{ind},1}}{R_{\mathrm{ind},1} + \frac{1}{K_u S_{\mathrm{coil}}} \frac{\mathrm{MLT}}{\sigma_w} + K_u S_{\mathrm{coil}} r_w^2 \frac{1}{\sigma_w \delta_w^4} \left\langle 2\pi r \left| \bar{\mathbf{H}}_{o,1} \right|^2 \right\rangle_{S_{\mathrm{coil}}}}. \tag{26}$$

From the design point of view, it is of interest to calculate the strand radius, which provides the optimum efficiency at a fixed frequency considering the geometry restrictions $r_{w,\mathrm{opt,ava}}$ and also considering the system geometry. This radius can be obtained by applying the condition $\partial \eta_{\mathrm{ind,ava}}^{\mathrm{LF}} / \partial r_w = 0$ in (26), resulting in the following expression:

$$r_{w,\mathrm{opt,ava}} = \left(\sqrt{\frac{b}{b+2} \frac{\mathrm{MLT}}{\left\langle 2\pi r \left| \bar{\mathbf{H}}_{o,1} \right|^2 \right\rangle} \frac{(r_a)^b \delta_w^2}{S_{\mathrm{coil}}}} \right)^{\frac{1}{(b+1)}}. \tag{27}$$

The optimum efficiency achieved with these strands, $\eta_{\mathrm{ind,opt,ava}}$, can be calculated by inserting $r_{w,\mathrm{opt,ava}}$ in (26). Fig. 9 shows a set of curves of the induction efficiency with respect to the frequency for different strands when winding restrictions are considered. The envelope of the complete set of

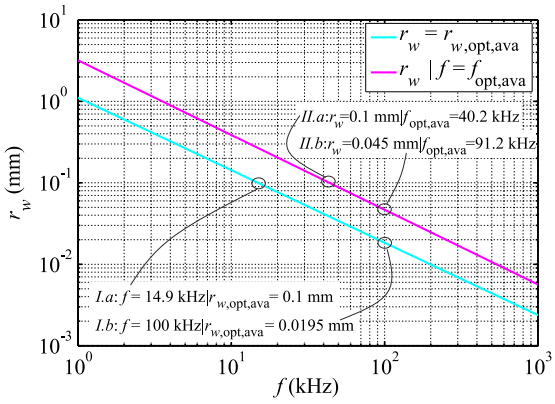

Fig. 10. Strand radius for achieving the maximum efficiency without geometrical restrictions (cyan line) and the optimum available efficiency $\eta_{\mathrm{ind,opt,ava}}$ (magenta line) at a given frequency.

curves defines the optimum available efficiency at different frequencies for the strand radii given in (27). It is interesting to remark that at the LF range, the thicker the wire, the higher the efficiency; whereas at the HF range, it is inferred that the efficiency can be improved by using finer strands.

Regarding the set of curves in Fig. 9, for a fixed strand radius a frequency can be calculated at which the efficiency is optimized. This frequency is called $f_{\mathrm{opt,ava}}$ because the geometry restrictions are also considered. As in the previous section, this frequency is obtained by numerical processing. In Fig. 9, the magenta line represents the peaks of efficiency for different strand radii. As in the previous section, the efficiencies at $f_{\mathrm{opt,ava}}$ are lower than the envelope curve called $\eta_{\mathrm{ind,opt,ava}}$. This fact can be explained by means of an example. The peak efficiency of the strand radius $r_w = 0.05$ mm that is obtained at $f_{\mathrm{opt,ava}} = 90$ kHz is slightly higher than 96%. However, the cyan curve indicates that a $\eta_{\mathrm{ind,opt,ava}} \approx 96.8\%$ could be achieved at $f =$ 90 kHz by using a strand with a radius smaller than $r_w = 0.05$ mm. Some results that could help when selecting the strand radius for optimal efficiency at a fixed frequency are given in the next section.

E. Selection of the Strand Radii at a Fixed Frequency

Usually, the switching frequency of a specific application is fixed or bounded by different reasons, and therefore, the strand radius should be selected according to an optimal efficiency criterion. Fig. 10 shows the strand radii corresponding to the envelope and peak of efficiency curves, called $r_{w,\mathrm{opt,ava}}$ and $r_w|f_{\mathrm{opt,ava}}$, respectively. According to this figure, the strand radius $r_w = 0.1$ mm is the best option at a fixed frequency of $f = 14.9$ kHz. On the other hand, at $f = 100$ kHz, the highest efficiency corresponds to $r_w = 19.5\,\mu$m. Therefore, this figure shows that the higher the frequency, the smaller the radius. However, this choice could lead to small radius and expensive designs. Considering that the cost of the litz wire greatly depends on the strand diameter, several authors have proposed design methods including not only the efficiency but also the cost [15].

F. Practical Design Guidance

Next, a guidance of possible methodology intended to optimize the efficiency of an induction heating system is presented. This guidance is based on the optimization of different scenarios with different specifications. Two different cases, called *a* and *b*, are considered in each scenario.

Table II summarizes these scenarios and also includes the specified parameters (highlighted by gray), the equations to be used in each case, the resulting parameters of the calculations, and the pertinent figures of the optimization. For this reason, the ordinal number of scenarios and cases also corresponds to the labels that appear in curves of Figs. 5, 6, and 8–10. The optimization carried out in some scenarios is explained as follows.

Scenario I corresponds to an optimization case in which the frequency is specified and the radius of the strand, the number of turns and the number of strands for maximum efficiency have to be determined. In this case, the strand radius is calculated by means of (27). Once $r_{w,\mathrm{opt,ava}}$ is calculated, the available product of the number of turns by the number of strands is calculated by means of (25). The achieved efficiency at this design is obtained by using (26). In the Scenario II, the radius of the strand is specified and the optimization consists of calculating the frequency, the number of strands and turns that maximizes the efficiency. Scenario III corresponds to a case where the prototype geometry is specified and the optimization consists of determining the optimum frequency. Finally, in scenario IV, the copper volume that optimizes the efficiency for a given strand radius and frequency is determined. This optimization is often required for the magnetic design of SMPS.

Before ending this Section, it is worth to comment some aspects of the design of solenoidal arrangements [see Fig. 3(b)] because its design is more similar to the magnetic design for SMPS than planar arrangements [see Fig. 3(a)]. In magnetic design for SMPS, it is usual to consider if a specific design fits in a smaller bobbin in order to reduce the size of the application. Redesigns usually lead to changes of some parameters, as the frequency or the strand radius. Similarly, the effect of the external radius of the solenoidal arrangement of Table III (whose internal radius is $r_{\mathrm{int}} = 12.5$ mm) is analyzed by means of the presented method. The results are presented in Fig. 11. As is shown, designs with smaller external radii can be obtained by increasing the operating frequency. In general, it is also observed that at a fixed frequency, the increase of the external radius lead to a reduction of the efficiency.

IV. Experimental Verification

A. Small-Signal Tests

Several planar and solenoidal coils were built in order to verify the previous results. A picture of both arrangements is depicted in Fig. 12. For both configurations, three prototypes with different numbers of turns, strands, and constant nn_{s} were tested. The parameters of the prototypes are presented in Table III. For the solenoidal configuration, the manufactured nn_{s} factor was 1200.

TABLE II
PRACTICAL DESIGN EXAMPLES INCLUDING GEOMETRY RESTRICTIONS∗

Scenario I: Maximum Efficiency Design Given the Frequency					
Parameter	Case-I.a	Case-I.b	Calculation	Equation	Figure
f	14.9 kHz	100.0 kHz	Specification	–	–
r_w	100 μm	19.5 μm	$r_{w,\mathrm{opt,ava}}$	(27)	Fig. 10
nn_s	1764	35800	$nn_{s,\mathrm{ava}}\|r_w = r_{w,\mathrm{opt,ava}}$	(25)	Fig. 6
η_{ind}	93.0%	96.9%	$\eta^{LF}_{\mathrm{ind,ava}}\|r_w = r_{w,\mathrm{opt,ava}}, f$	(26)	Fig. 9
Scenario II: Frequency Design for Maximum Efficiency Given the Wire Radius					
Parameter	Case-II.a	Case-II.b	Calculation	Equation	Figure
f	40.2 kHz	90.0 kHz	$f = f_{\mathrm{opt,ava}}$	$\partial\eta_{\mathrm{ind,ava}}/\partial f = 0$	Fig. 9
r_w	100 μm	50 μm	Specification	–	–
nn_s	1764	6450	$nn_s\|f = f_{\mathrm{opt,ava}}, r_w$	(25)	Fig. 6
η_{ind}	94.8%	96.3%	$\eta^{LF}_{\mathrm{ind,ava}}\|f = f_{\mathrm{opt,ava}}, r_w$	(26)	Fig. 9
Scenario III: Frequency Design for a Fixed Prototype					
Parameter	Case-III.a	Case-III.b	Calculation	Equation	Figure
f	61.4 kHz	175 kHz	$f = f_{\mathrm{opt}}$	$\partial\eta_{\mathrm{ind}}/\partial f = 0$	Fig. 5
r_w	100 μm	100 μm	Specification	–	–
nn_s	1200	400	Specification	–	–
η_{ind}	94.0%	90.2%	$\eta_{\mathrm{ind}}\|f = f_{\mathrm{opt}}, nn_s, r_w$	(21)	Fig. 5
Scenario IV: Optimal Copper Volume Design Given Wire Radius and Frequency					
Parameter	Case-IV.a	Case-IV.b	Calculation	Equation	Figure
f	10 kHz	300 kHz	Specification	–	–
r_w	100 μm	100 μm	Specification	–	–
nn_s	1764	388	$nn_{s,\max} \leq nn_{s,\mathrm{ava}}$	(18), (25)	Fig. 6
η_{ind}	94%	89.2%	$\eta_{\mathrm{ind,max}}, \eta_{\mathrm{ind,ava}}$	(19)	Fig. 8

∗ Fixed parameters are highlighted in gray.

TABLE III
GEOMETRY OF THE PROTOTYPES

Definition	Symbol	Planar Configuration	Solenoidal Configuration
Coil internal radius	r_{int}	17.5 mm	12.5 mm
Coil external radius	r_{ext}	32.5 mm	15.5 mm
Coil thickness	t	4.5 mm	38.0 mm
Distance coil load	d_l	6.0 mm	8.0 mm
Thickness load	t_l	4.0 mm	4.5 mm
Distance coil flux-concentrator	d_f	1.0 mm	-
Flux concentrator thickness	t_f	4.5 mm	-
Wire radius	r_w	0.1 mm	0.1 mm
Factor nn_s	nn_s	960	1200

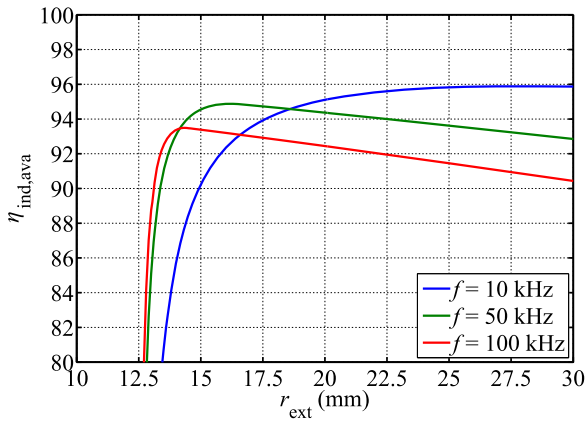

Fig. 11. Available efficiency, $\eta_{\mathrm{ind,ava}}$ of the solenoidal induction heating system with respect to the external radius of the coil at different frequencies given a wire radius equals to $r_w = 0.1$ mm.

The small-signal tests consisted of resistance measurements and comparisons with the results of the model described in the Section II. The resistance was measured by means of a high-precision Agilent E4980A LCR meter. The signal level was set to 10 mA and the frequency was ranged between 1 kHz and 2 MHz. Coils were measured in different scenarios that include different media. The media properties are presented in Table IV.

Fig. 13(a) shows experimental and calculated resistance for the three planar coils with constant nn_s in air. Moreover, Fig. 13 (b) shows experimental and calculated resistances for the three planar coils placed between a conductive media (the workpiece) and the flux concentrator. The experimental and calculated resistances for solenoidal coils in air and with the target load are presented in Fig. 14(a) and (b), respectively. In general, a good

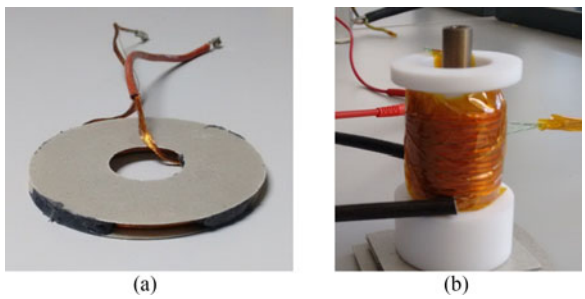

Fig. 12. Experimental arrangements. (a) Planar. (b) Solenoidal.

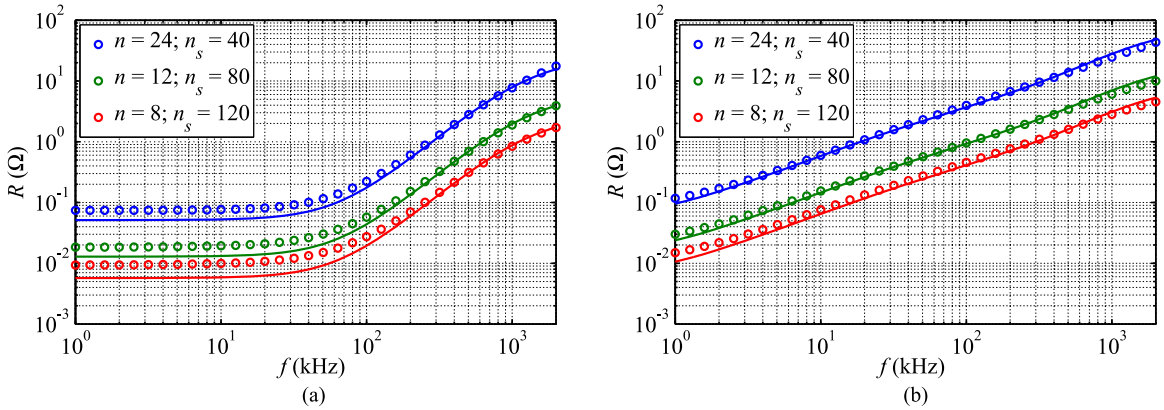

Fig. 13. Experimental (circle mark) and calculated (continuous line) resistance values for the planar configuration. (a) Coils in air. (b) Planar coils between a magnetic substrate and a load.

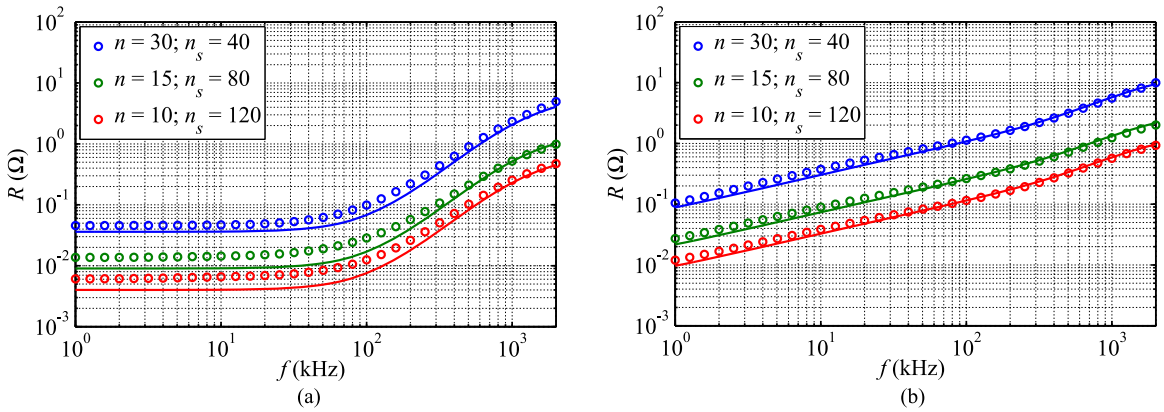

Fig. 14. Experimental (circle mark) and calculated (continuous line) resistance values for the solenoidal configuration. (a) Coils in air. (b) Coils with load.

TABLE IV
MEDIA CHARACTERISTICS

Medium	Relative permeability, μ_r	Electric conductivity, σ
Air	1	0
Flux concentrator	2000	0
Planar load	170	8e6 [S/m]
Solenoidal Load	150	8e6 [S/m]

agreement is observed between the measured and calculated results in the different tested configurations, which confirm the accuracy of the proposed model. Moreover, considering the experimental verification, the discrepancy observed at LF in the resistance of some configurations in air is associated with the low resistance values at the LF range, i.e., tens of mΩ. At this frequency range, the resistance of the coil almost corresponds to the dc resistance, and therefore, measurements are affected by the setup arrangement, as the proper connection of all strands, length of the terminals, among others.

Figs. 15 and 16 show the experimental and calculated values of the inductive efficiency for the prototypes with planar and solenoidal configurations, respectively. The experimental results were obtained according to the method proposed in [21],

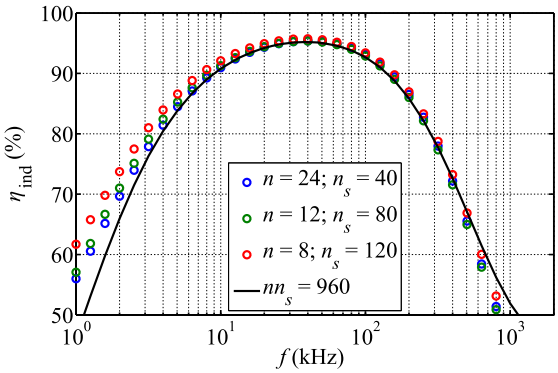

Fig. 15. Induction efficiency for the planar configuration. Experimental-calculated (circle mark) and calculated (continuous line) values.

which combines the results shown in the previous figures to obtain the experimental efficiency values. This method assumes that the calculated $R_{\rm ind}$ can be used for estimating the experimental efficiency if the total measured resistance matches with calculations. According to Figs. 15 and 16, coils with constant $nn_{\rm s}$ (and for the same wire radius) have the same induction efficiency. This result is valid for both planar and solenoidal configurations.

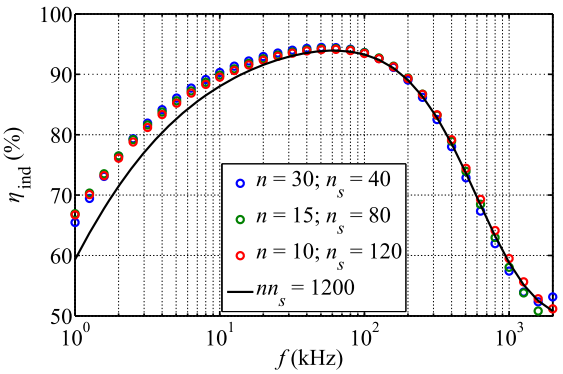

Fig. 16. Induction efficiency for the solenoidal configuration. Experimental-calculated (circle mark) and calculated (continuous line) values.

B. Test Under Real Working Conditions

The litz wire has been used in induction cooking much more widely than in industrial induction heating. There are several reasons for this, mainly derived from the superior thermal performance of copper tubes such as high-temperature operation and possibility of cooling. Other reasons are the low cost of copper tubes and the limitations of the litz wire above 1 MHz [38]. However, in industrial applications with lower thermal requirements, low operation frequency or oriented to high-efficiency performance, a litz wire could compete with copper tubes.

A solenoidal coil in real working conditions was tested with the purpose of verifying if a litz wire is a feasible option for application in several induction systems. The solenoidal coil consisted of $n = 30$ turns, which were wound with a cable of $n_s = 40$ strands of $r_w = 0.1$ mm, i.e. $nn_s = 1200$. The coil was fed by a half-bridge series resonant inverter. The switching frequency at resonance was equal to the optimum operation frequency $f_{\rm opt} = 61.4$ kHz for the considered design. Other parameters of the setup were: resonant capacitor $C_r = 600$ nF, dc bus voltage amplitude $V_{\rm dc} = 50$ V, and output power $P_o = 500$ W [28]. The equivalent circuit of the converter connected to the induction heating system and the main waveforms captured are represented in Fig. 17. According to the waveform of the inductor current i_o, it can be deduced that the first harmonic current contains most power. In these applications with resonant converters working near the resonant frequency, it is often considered that the first harmonic carries up to the 95% of the total power [39].

Moreover, thermocouples have been placed in outermost turns ($T_{\rm wire,1}$, $T_{\rm wire,2}$) and in the internal wall of the bobbin ($T_{\rm bobbin}$). Several tests were carried out. The location of the thermocouples is pointed out and the measured temperatures after 40 s at nominal power are depicted in Fig. 18. The peak temperature is reaches after switches OFF the power due to the convection and radiation heat contributions.

Furthermore, Fig. 19 shows a picture of the prototype in real working conditions in different times (20, 30, and 40 s) along the test realized. These tests correspond to an extreme case where the workpiece is heated up to red hot (about 800 °C). However, according to Fig. 18 the temperature of both the copper and the bobbin is lower. As it was commented in the introduction, low-emissive materials for the bobbin help to not exceed the self-heating of the windings.

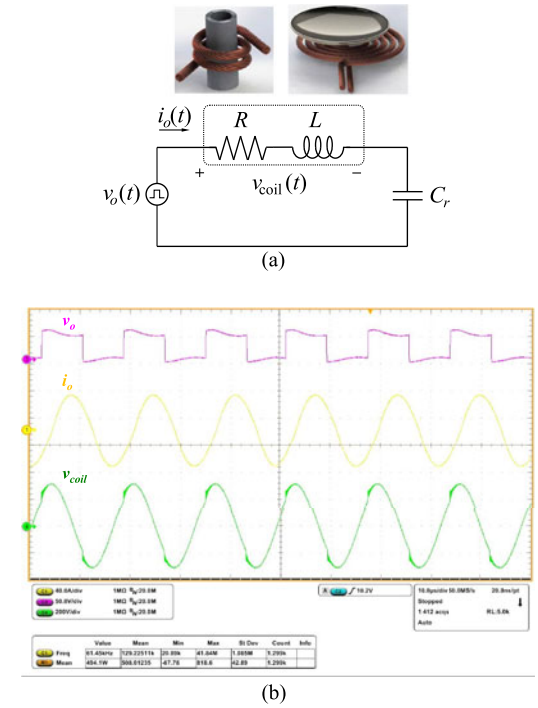

Fig. 17. Resonant converter connected to an inductor heating system. (a) Equivalent circuit of the converter. (b) Oscilloscope capture of the main waveforms.

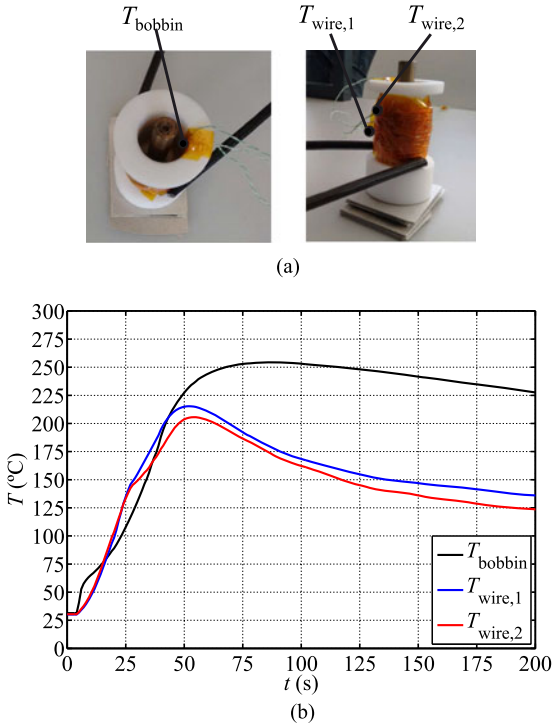

Fig. 18. Thermal measurements. (a) Thermocouples location. (b) Thermal measurements.

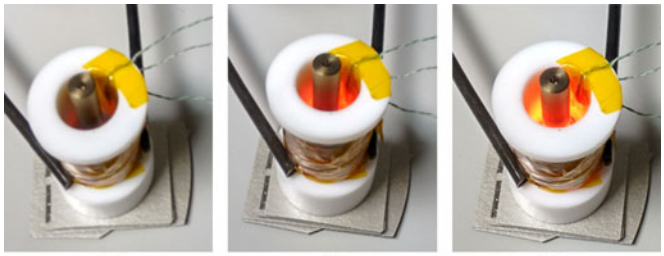

Fig. 19. Pictures of the solenoidal coil in real working conditions. (a) $t = 20$ s. (b) $t = 30$ s. (c) $t = 40$ s.

V. Conclusion

This paper presents an analysis of the efficiency of litz-wire induction heating systems with respect to the frequency and geometry parameters (number of turns, number of strands, and wire radius). The analysis reveals that the induction efficiency could be maximized with respect to the number of turns multiplied by the number of strands (which is equivalent to the copper volume) for fixed frequency and strand diameter. Moreover, an optimization of the induction efficiency with respect to the operation frequency for a given coil geometry is also derived by means of a postprocessing tool. Furthermore, strand radius selection criteria have been provided and the optimum wire radius maximizing the inductive efficiency under geometry restrictions is also investigated. Finally, several measurements have been carried out in order to verify the proposed calculation method.

References

[1] X. Wang, J. Tang, and L. Shi, "Induction heating of magnetic fluids for hyperthermia treatment," *IEEE Trans. Magn.*, vol. 46, no. 4, pp. 1043–1051, Apr. 2010.

[2] P. D. Barba, F. Dughiero, and E. Sieni, "Magnetic field synthesis in the design of inductors for magnetic fluid hyperthermia," *IEEE Trans. Magn.*, vol. 46, no. 8, pp. 2931–2934, Aug. 2010.

[3] H. N. Pham, H. Fujita, K. Ozaki, and N. Uchida, "Dynamic analysis and control for resonant currents in a zone-control induction heating system," *IEEE Trans. Power Electron.*, vol. 28, no. 3, pp. 1297–1307, Mar. 2013.

[4] F. Dughiero, M. Forzan, C. Pozza, and E. Sieni, "A translational coupled electromagnetic and thermal innovative model for induction welding of tubes," *IEEE Trans. Magn.*, vol. 48, no. 2, pp. 483–486, Feb. 2012.

[5] H. N. Pham, H. Fujita, K. Ozaki, and N. Uchida, "Phase angle control of high-frequency resonant currents in a multiple inverter system for zone-control induction heating," *IEEE Trans. Power Electron.*, vol. 26, no. 11, pp. 3357–3366, Nov. 2011.

[6] J. Acero, C. Carretero, O. Lucia, R. Alonso, and J. M. Burdio, "Mutual impedance of small ring-type coils for multiwinding induction heating appliances," *IEEE Trans. Power Electron.*, vol. 28, no. 2, pp. 1025–1035, Feb. 2013.

[7] C. R. Sullivan and L. Beghou, "Design methodology for a high-Q self-resonant coil for medical and wireless-power applications," in *Proc. IEEE Workshop Control Model. Power Electron.*, 2013, pp. 1–8.

[8] M. Bartoli, A. Reatti, and M. K. Kazimierczuk, "Minimum copper and core losses power inductor design " presented at the Industry Applications Annu. Meet. Conf., San Diego, CA, USA, 1996.

[9] H. Rossmanith, M. Doebroenti, M. Albach, and D. Exner, "Measurement and characterization of high frequency losses in nonideal litz wires," *IEEE Trans. Power Electronics*, vol. 26, no. 11, pp. 3386–3394, Nov. 2011.

[10] R. P. Wojda and M. K. Kazimierczuk, "Winding resistance of litz-wire and multi-strand inductors," *IET Elect. Power Appl.*, vol. 5, pp. 257–268, Nov. 2012.

[11] H. Hamalainen, J. Pyrhonen, J. Nerg, and J. Talvitie, "AC resistance factor of litz-wire windings used in low-voltage high-power generators," *IEEE Trans. Ind. Electron.*, vol. 61, no. 2, pp. 693–700, Feb. 2014.

[12] D. C. Meeker, "An improved continuum skin and proximity effect model for hexagonally packed wires," *J. Comput. Appl. Math.*, vol. 236, pp. 4635–4644, Dec. 2012.

[13] C. R. Sullivan, "Computationally efficient winding loss calculation with multiple windings, arbitrary waveforms, and two-dimensional or three-dimensional field geometry," *IEEE Trans. Power Electron.*, vol. 16, no. 1, pp. 142–150, Jan. 2001.

[14] C. R. Sullivan, "Optimal choice for number of strands in a litz-wire transformer winding," *IEEE Trans. Power Electron.*, vol. 14, no. 2, pp. 283–291, Mar. 1999.

[15] C. R. Sullivan, "Cost-constrained selection of strand diameter and number in a litz-wire transformer winding," *IEEE Trans. Power Electron.*, vol. 16, no. 2, pp. 281–288, Mar. 2001.

[16] J. D. Pollock, T. Abdallah, and C. R. Sullivan, "Easy-to-use CAD tools for litz-wire winding optimization," in *Proc. IEEE Appl. Power Electron. Conf. Expo.*, 2003, pp. 1157–1163.

[17] C. R. Sullivan and R. Y. Zhang, "Simplified design method for litz wire," in *Proc. IEEE Appl. Power Electron. Conf. Expo.*, 2014, pp. 2667–2674.

[18] A. Stadler, "The optimization of high frequency inductors with litz-wire windings," in *Proc. IEEE Conf. Compat. Power Electron.*, Ljubljana, Slovenia, 2013, pp. 209–213.

[19] J. Acero, R. Alonso, J. M. Burdío, L. A. Barragán, and D. Puyal, "Frequency-dependent resistance in litz-wire planar windings for domestic induction heating appliances," *IEEE Trans. Power Electron.*, vol. 21, no. 4, pp. 856–866, Jul. 2006.

[20] G. Cerri, S. A. Kovyryalov, and V. M. Primiani, "Modelling of a litz-wire planar winding geometry for an accurate reactance evaluation," *IET Sci., Meas. Technol.*, vol. 4, pp. 214–219, Jul. 2010.

[21] J. Acero, C. Carretero, R. Alonso, and J. M. Burdío, "Quantitative evaluation of induction efficiency in domestic induction heating applications," *IEEE Trans. Magn.*, vol. 49, no. 4, pp. 1382–1389, Apr. 2013.

[22] J. Acero, J. M. Burdío, L. A. Barragán, D. Navarro, R. Alonso, J. R. García, F. Monterde, P. Hernández, S. Llorente, and I. Garde, "Domestic induction appliances," *IEEE Ind. Appl. Mag.*, vol. 16, no. 2, pp. 39–47, Mar./Apr. 2010.

[23] O. Lucia, J. Acero, C. Carretero, and J. M. Burdio, "Induction heating appliances: Toward more flexible cooking surfaces," *IEEE Ind. Electron. Mag.*, vol. 7, no. 3, pp. 35–47, Sep. 2013.

[24] I. Lope, C. Carretero, J. Acero, R. Alonso, and J. M. Burdio, "Frequency-dependent resistance of planar coils in printed circuit board with litz structure," *IEEE Trans. Magn.*, vol. 50, no. 12, pp. 1–9, Dec. 2014.

[25] I. Lope, C. Carretero, J. Acero, R. Alonso, and J. M. Burdio, "AC power losses model for planar windings with rectangular cross-sectional conductors," *IEEE Trans. Power Electron.*, vol. 29, no. 1, pp. 23–28, Jan. 2014.

[26] C. Feeney, N. Wang, S. C. OMathuna, and M. Duffy, "A 20-MHz 1.8-W DC-DC converter with parallel microinductors and improved light-load efficiency," *IEEE Trans. Power Electron.*, vol. 30, no. 2, pp. 771–779, Feb. 2015.

[27] C. Feeney, N. Wang, S. Kulkarni, Z. Pavlovic, C. O Mathuna, and M. Duffy, "Loss modeling of coupled stripline microinductors in power supply on chip applications," *IEEE Trans. Power Electron.*, vol.PP, no.99, pp. 1–1.

[28] H. Sarnago, O. Lucia, A. Mediano, and J. M. Burdio, "Analytical model of the half-bridge series resonant inverter for improved power conversion efficiency and performance," *IEEE Trans. Power Electron.*, vol. 30, no. 8, pp. 4128–4143, Aug 2015.

[29] C. Carretero, O. Lucia, J. Acero, and J. M. Burdio, "Computational modeling of two partly coupled coils supplied by a double half-bridge resonant inverter for induction heating appliances," *IEEE Trans. Ind. Electron.*, vol. 60, no. 8, pp. 3092–3105, Aug. 2013.

[30] J. A. Ferreira, *Electromagnetic Modelling Power Electronic Converters*. Norwell, MA, USA: Kluwer, 1989.

[31] C. Carretero, J. Acero, and R. Alonso, "TM-TE decomposition of power losses in multi-stranded litz-wires used in electronic devices," *Progress Electromagn. Res.*, vol. 123, pp. 83–103, Dec. 2012.

[32] J. Gyselinck and P. Dular, "Frequency-domain homogenization of bundles of wires in 2-D magnetodynamic FE calculations," *IEEE Trans. Magn.*, vol. 41, no.5, pp. 1416–1419, May 2005.

[33] X. Nan and C. R. Sullivan, "An improved calculation of proximity-effect loss in high-frequency windings of round conductors," in *Proc. IEEE Power Electron. Spec. Conf.*, 2003, pp. 853–860.

[34] X. Nan and C. R. Sullivan, "Simplified high-accuracy calculation of eddy-current loss in round-wire windings," in *Proc. IEEE Power Electron. Spec. Conf.*, 2004.

[35] R. P. Wojda and M. K. Kazimierczuk, "Analytical optimization of solid-round-wire windings," *IEEE Trans. Ind. Electron.*, vol. 60, no. 3, pp. 1033–1041, Mar. 2013.
[36] M. K. Kazimierczuk, *High Frequency Magnetic Components*, 2nd ed. New York, NY, USA: Wiley, 2009.
[37] W. G. Hurley and W. H. Wölfle, *Transformers and Inductors for Power Electronics. Theory, Design and Applications*. Chichester, U.K.: Wiley, 2013.
[38] C. R. Sullivan, "Layered foil as an alternative to litz wire: Multiple methods for equal current sharing among layers," in *Proc. IEEE Workshop Control Model. Power Electron.*, 2014, pp. 1–7.
[39] J. Jordan, V. Esteve, E. Sanchis-Kilders, E. J. Dede, E. Maset, J. B. Ejea, and A. Ferreres, "A comparative performance study of a 1200 V Si and SiC MOSFET intrinsic diode on an induction heating inverter," *IEEE Trans. Power Electron.*, vol. 29, no. 5, pp. 2550–2562, May 2014.

Ignacio Lope (S'09) received the M.Sc. degree in electrical engineering and the Ph.D. degree in power electronics from the University of Zaragoza, Zaragoza, Spain, in 2010 and 2015, respectively.

He is currently with the BSH Home Appliances Spain, Zaragoza, involved in several projects focused on developing domestic induction heating appliances. His current research interests include electromagnetic modeling of inductive coupled contactless energy transfer systems, and loss modeling of magnetic devices.

Dr. Lope received the Prize Letter Award for 2014 in the IEEE TRANSACTIONS ON POWER ELECTRONICS.

Jesús Acero (M'06) received the M.Sc. and Ph.D. degrees in electrical engineering from the University of Zaragoza, Zaragoza, Spain, in 1992 and 2005, respectively.

From 1992 to 2000, he worked in several industry projects, especially in custom power supplies for research laboratories. Since 2001, he has been with the Department of Electronic Engineering and Communications, University of Zaragoza, Zaragoza, where he is currently an Associate Professor. His main research interests include resonant converters for induction heating applications, inductive-type load modeling, and magnetics.

Dr. Acero has been an Associate Editor of the IEEE TRANSACTIONS ON POWER ELECTRONICS since 2015. Dr. Acero is a member of the Aragon Institute for Engineering Research (I3A).

Claudio Carretero (M'11) received the M.Sc. degree in physics and the Ph.D. degree in electrical engineering from the University of Zaragoza, Zaragoza, Spain, in 2002 and 2010, respectively.

He is currently an Assistant Professor in the Department of Physics Applied, University of Zaragoza. His main research interests include induction-heating applications and electromagnetic modeling of induction systems.

Dr. Carretero is a member of the Aragon Institute for Engineering Research (I3A).